# An experimental study to explore hydrogen diffusion in clinopyroxene at low temperatures (195 – 400 °C) and consequences for re-equilibration at near surface conditions

Thilo Bissbort[1,3], Kendra J. Lynn*[,2], Hans-Werner Becker[3], Sumit Chakraborty[1,3]

[1]Institute for Geology, Mineralogy and Geophysics, Ruhr-University Bochum, Germany
[2] Department of Earth Sciences, University of Delaware, USA
* now at Hawaiian Volcano Observatory, United States Geological Survey, USA
[3]Central Unit for Ionbeams and Radionuclides RUBION, Ruhr-University Bochum, Germany

**Corresponding author:** Thilo Bissbort (thilo.bissbort@rub.de)

**Key Points:**

- Diffusion rates of hydrogen in clinopyroxene in the low temperature range (195 – 400 °C) were quantified for the first time
- Diffusion coefficients at low temperatures lie within the range of extrapolations from high temperature experiments
- Non-isothermal modeling was applied to evaluate potential re-equilibration of clinopyroxene crystals at low temperatures

## Abstract

Studying diffusion of hydrogen in nominally anhydrous minerals (NAMs), like clinopyroxene, at low temperatures is a challenging task due to experimental and analytical difficulties. We applied a combination of hydrogen implantation to produce concentration gradients in natural diopside crystals with Nuclear Resonance Reaction Analysis (NRRA) measurements of nanoscale diffusion profiles. Thereby, we were able to conduct experiments at temperatures between 195 – 400 °C. Obtained diffusion rates show a consistent Arrhenius relation $D_H = 5.47 (\pm 13.98) \cdot 10^{-8} \cdot exp\ (-115.64\ (\pm 11.5)\ kJ\ mol^{-1}\ /RT)\ m^2 s^{-1}$. Notably, our results lie well within the range of extrapolations from high temperature experiments (≥ 600 °C) of previous studies. This implies that fast diffusion of hydrogen (compared to other elements) extends to low temperatures. We used these results in a non-isothermal diffusion model that simulates the ascent of crystals (0.5, 1.0, and 2.0 mm) along two representative geotherms (oceanic and continental) from 600 to 100 °C, to assess potential re-equilibration of H contents in clinopyroxene at low temperatures. Our model highlights the need to carefully consider

boundary conditions, which are a function of P-T-$fO_2$, that control the concentration gradient at the crystal's rim. The results from this model allow an assessment when re-equilibration in dependence of crystal size and cooling rate must be considered. Fast ascent (e.g., kimberlitic melt) preserves initial hydrogen contents even in 0.5 mm size clinopyroxene crystals. However, dwelling at low temperatures (e.g., 300 °C) for several thousands of years (e.g., serpentinization) leads to extensive re-equilibration in 2 mm crystals.

# 1 Introduction

The presence of hydrogen (often simplistically termed "water") in nominally anhydrous minerals (NAMs) has considerable implications for our understanding of Earth's dynamics. Properties such as melting (Hirth and Kohlstedt 1996), electrical conductivity (Karato 1990; Fei *et al.* 2020), seismic response (Karato and Jung 1998), phase transitions (Ohtani and Litasov 2006), and mechanical features (Chen *et al.* 2006) of a mineral are affected already by trace amounts of hydrogen. Although measured concentrations of H in NAMs are very low (e.g., a few to several thousand ppm $H_2O$, typically; e.g., Bell and Rossman 1992; Warren and Hauri 2014; Le Roux *et al.* 2021) compared to those in common hydrous phases, when the hydrogen contents of a single mineral are scaled to a planetary scale it becomes obvious that the amount of hydrogen that might be stored in the mantle would make a large contribution to the earth's overall water budget and cycle (e.g., Hirschmann 2006; Hirschmann and Kohlstedt 2012). Thus, it is not surprising that great efforts have been invested in further exploring the role of hydrogen in NAMs since the early works of Martin and Donnay (1972), as reflected in *Volume 62* of *Reviews in Mineralogy and Geochemistry* (Keppler and Smyth 2006) and a vast number of more recent studies (e.g., Padrón-Navarta *et al.* 2014; Tollan *et al.* 2017; Ferriss *et al.* 2018; Reynes *et al.* 2018; Thoraval *et al.* 2019; Liu and Yang 2020; Moine *et al.* 2020; Demers-Roberge *et al.* 2021; Jollands *et al.* 2021).

However, a legitimate question that remains is whether hydrogen concentrations that are measured in NAMs collected on Earth's surface really represent the original H contents established in the mantle, or if these contents were modified at some later stage e.g., by alteration, metasomatism (Kilgore *et al.* 2020; Tang *et al.* 2020; Peslier *et al.* 2015) or mineral-melt interaction (Lynn and Warren 2021; Le Roux *et al.* 2021). In spite of the growing number of experimental studies that reveal new details on hydrogen in NAMs and systematic studies about hydrogen contents in these minerals (Warren and Hauri 2014; Kumamoto *et al.* 2019),

studies that treat natural mantle xenoliths seem to yield contrasting results in terms of what the hydrogen content actually recorded (Gose *et al.* 2011; Wang *et al.* 2021). Since diffusion controls the redistribution of hydrogen in a crystal it is crucial to determine rates of diffusive transport as a function of various parameters (e.g., temperature, pressure, $fO_2$, or mineral composition) to assess potential modifications of hydrogen contents at different conditions. These quantities are known only by extrapolation of high temperature data because most experimental data for H diffusion in NAMs have been collected only over a limited range of high temperatures (800-1200°C for olivine, 600-1000°C for pyroxenes; e.g., Demouchy and Mackwell 2006; Demouchy *et al.* 2016; Ferriss *et al.* 2018; Mackwell and Kohlstedt 1990; Ferriss *et al.* 2016; Hercule and Ingrin 1999; Ingrin *et al.* 1995; Stalder and Skogby 2003; Woods *et al.* 2000; Stalder and Behrens 2006) and may lead to large uncertainties on extrapolation (Lynn and Warren 2021).

To quantify the loss / retention of hydrogen at low temperatures (e.g., <<600°C) it is necessary to know the rates of diffusion at those conditions. We combined two experimental methods, ion implantation and Nuclear Resonance Reaction Analysis (NRRA), to develop a method for the determination of diffusion rates of H in NAMs at low temperatures. Hereby we were able to quantify diffusion rates of hydrogen in clinopyroxene at 195-400 °C, temperatures that are associated with metasomatism, prolonged cooling of lava flows or eruption deposits, and serpentinization and that are relevant for applications such as ascent chronometry (e.g., Newcombe *et al.* 2020; Jollands *et al.* 2020). We use non-isothermal diffusion modeling with the newly obtained diffusion rates to assess the feasibility of hydrogen re-equilibration during ascent of clinopyroxene from the mantle.

# 2 Methods

## 2.1 Sample preparation

For our diffusion experiments we used gem quality single crystals of diopsidic clinopyroxene. These had to have homogeneous surface areas that were free of cracks (to avoid adsorbed water causing artefacts) and could accommodate the ion beam used for NRRA analysis (spot ∅ 1-2 mm). The crystal used had an average formula of $Na_{0.03}Ca_{0.95}Mg_{0.88}Fe^{2+}_{0.08}Fe^{3+}_{0.02}Cr_{0.01}Al_{0.04}Si_{1.98}O_6$ (standard deviation of each formula unit

< 0.01). The composition was determined using a *Cameca SX Five FE* electron microprobe operated at 15 keV and 15 nA using wavelength dispersive spectrometers (Crystals used: LTAP for Na, Mg, TAP for Al, Si, LPET for K, Ti, PET for Ca, Cr and LLIF for Mn, Fe). $Fe^{2+}/Fe^{3+}$ ratios were estimated following Droop (1987). The standards used were jadeite (Na), San Carlos Olivine (Mg, Si), orthoclase (Al, K), diopside (Ca), rutile (Ti), synthetic $Cr_2O_3$ (Cr), spessartine (Mn), and fayalite (Fe). The crystallographic orientation was verified by Laue analysis before large prismatic crystals (few cm in length) were cut into several slabs (thickness ~ 3 mm) with the surface perpendicular to the crystallographic c-axis [001]. This was followed by embedding the samples in epoxy, grinding, and a final polishing (to 0.25 µm) using diamond paste. Cuboids with a surface area of about 4x4 mm were produced from these (Figure 1). Last, the samples were intensively cleaned using a routine involving deionized water, acetone, and ethanol and checked for the quality of polishing in an optical microscope.

### 2.2 Hydrogen implantation

Hydrogen was implanted at the 500 kV accelerator at the Central Unit for Ionbeams and Radionuclides (RUBION) at the Ruhr-University Bochum, Germany. The depth of the implantation depends on the ion beam energy and the material-specific stopping-power, *s*, which is an expression for the energy loss of the incident ion per distance unit (e.g., keV/nm). Concentration profiles were simulated using the software SRIM (Ziegler *et al.* 2010) prior to the actual implantation to determine the best choice of ion beam energy. Ideally, the latter is high enough to produce a concentration peak at depths far from the sample surface so that the profile after diffusion experiments is not (partially) superimposed by the surface peak that is related to adsorption of contaminants on the sample surface. Notably, we observed in another study that the process of preparation can introduce excess hydrogen in the near surface region in olivine (~ first 100 nm, Figure S3 supplementary material). Additionally, beam energies should be small enough to deposit hydrogen at depths that are still easily accessible using NRRA (max. depth ~ 2-3 µm). Fluences of $1.48 \cdot 10^{16}$ at/cm² were implanted at an ion energy of 60 keV and a beam intensity of 15 µA, while the implantation area was about 1 cm in diameter. The hydrogen source was a duoplasmatron and the ion beam was moved across the sample in a scanning mode during implantation to ensure homogeneous lateral distribution of

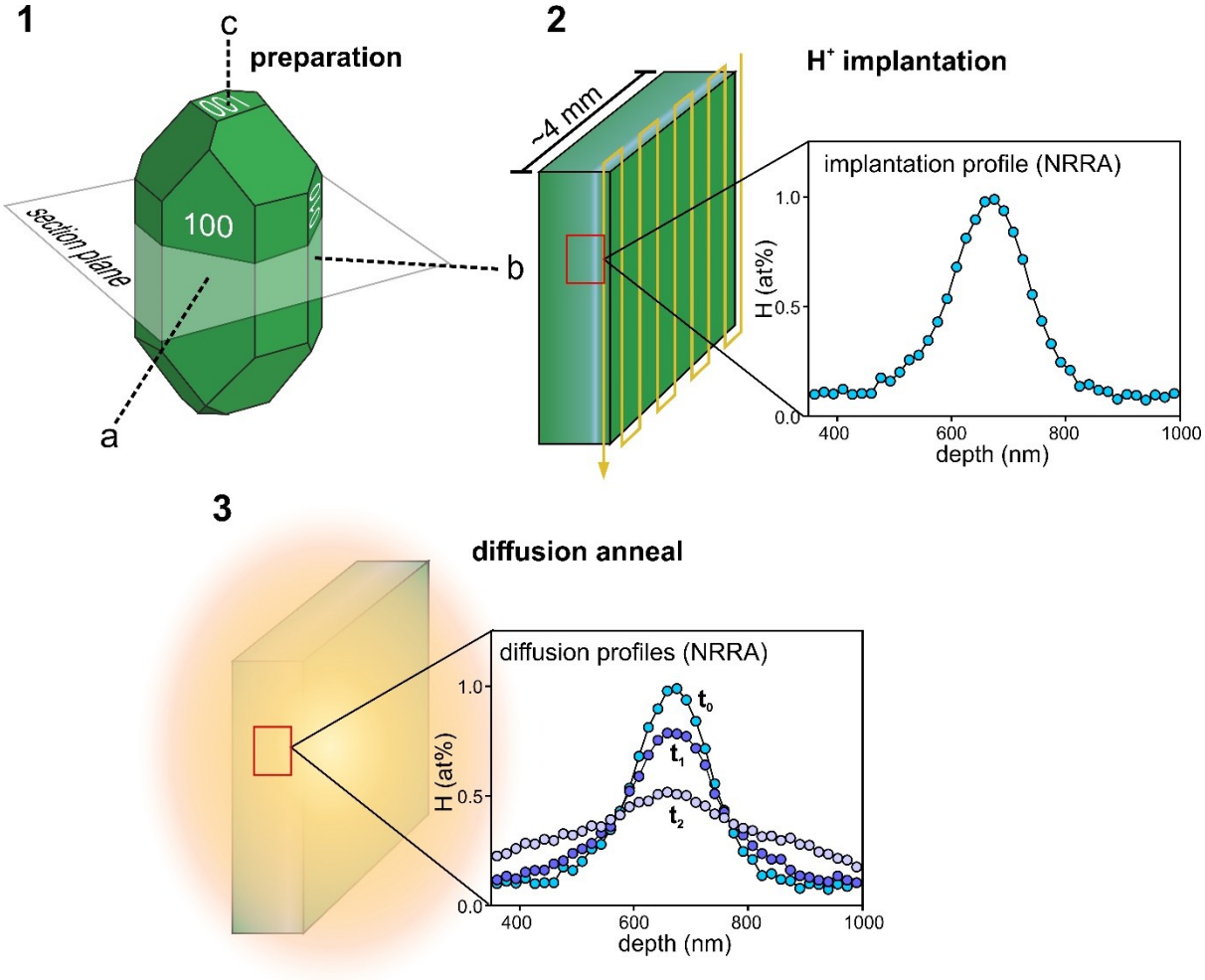


**Figure 1:** Illustration of the experimental procedure. (1) Diopside crystals were oriented and cuboids with a surface area of ca. 4x4 mm were cut with their surfaces perpendicular to the crystallographic c-axis (2) Polished sample surfaces were implanted by a hydrogen beam at 60 keV to produce concentration peaks at around 650 nm depth and 1 at% H (1650 $H_2O$ ppm wt%) concentration maxima. The beam width is larger than the sample size and the implantation is operated in a scanning mode (yellow line). (3) An analysis of the implantation profile by NRRA to precisely define the initial diffusion setup ($t_0$) was followed by diffusion anneals at 195 °C, 270 °C, and 400 °C in a gas mixing furnace (100 vol% $CO_2$). Resulting diffusion profiles were finally measured with NRRA. The non-destructive nature of the experimental design allows to obtain snapshots (profiles $t_1$ and $t_2$) of the proceeding homogenization with time. Dimensions are not to scale.

hydrogen (Figure 1). Implanted concentration maxima were located at around 650 nm from the sample surface.

### 2.3 Nuclear Resonance Reaction Analysis (NRRA)

Hydrogen concentration profiles that result from implantation and diffusion experiments were measured using Nuclear Resonance Reaction Analysis (NRRA). We limit the information about

this method to the essentials and refer the reader to Becker and Rogalla (2016) for a thorough description and to Bissbort *et al.* (2021) for an explanation in context of a diffusion study. NRRA utilizes the nuclear reaction $^{1}H(^{15}N,\alpha\gamma)^{12}C$ to detect hydrogen by bombarding the sample with $^{15}N$ ions. Emitted γ-rays have a specific energy of 4.4 MeV, which is characteristic for this nuclear reaction. The γ-rays are counted using a NaI(Tl) borehole detector with a high detection efficiency. The probability for the nuclear reaction depends strongly on the $^{15}N$ energy (width of the resonance window is 1.8 keV (Maurel and Amsel 1983)) with a resonance at 6393.6 ± 1.3 keV (Osipowicz *et al.* 1987) or at 6399.1 ± 2.9 keV (Becker *et al.* 1995). $^{15}N$ at the resonance energy will introduce the nuclear reaction in the very first atomic layers of the sample surface i.e., probe the hydrogen content at the surface. An increase in beam energy shifts the nuclear reaction to greater depths, since $^{15}N$ must loose energy by ion-sample-interaction first to attain the resonance energy. Hence, entire hydrogen depth profiles can be obtained by increasing the beam energy by small increments (e.g., 20 keV) while maintaining the depth resolution of a few nm due to the strong energy-sensitivity of the nuclear reaction. The detected γ-rays are normalized to the incident beam ions (= yield) and are a direct measure of the number of hydrogen atoms, thus making NRRA a standard-less technique. A conversion of the beam energy to a distance unit requires the knowledge of the material-specific stopping-power *s*, which is a function of the sample composition and density. We used the software SRIM (Ziegler *et al.* 2010) to calculate the stopping-power for $^{15}N$ in clinopyroxene of the relevant composition. Dividing the difference between beam energy and resonance energy (ΔE) by the stopping power yields the distance. Typical beam currents during analysis were ~40 nA. NRRA is a nuclear method that is independent of chemical bonds (which depend on outer electrons), thus the total hydrogen content is detected irrespective of its nature of bonding (e.g., $H_2$, $H_2O$, $(OH)^-$). One initial calibration is sufficient, and no standards are needed in contrast to alternative methods (e.g., SIMS or IR-spectroscopy) that are often used to measure hydrogen concentration profiles. Most notably, NRRA is a non-destructive technique that allowed us to measure the initial profile prior to experiments and to observe the development of diffusion profiles with time within one sample.

### 2.4 Hydrogen diffusion experiments

Implantation of hydrogen produced concentration profiles that are approximately described by a normal distribution with depth (depth of implantation maxima ~650 nm), with a minor excess of hydrogen along the surface-facing side of the concentration peak (Figure 2a). Hydrogen concentration depth profiles were obtained by NRRA in each sample after implantation and

before diffusion experiments, thereby allowing us to characterize the initial diffusion setup. Diffusion experiments were performed in a gas-mixing furnace using a K-type thermocouple (NiCr-Ni). The furnace was flushed with 100 vol% $CO_2$ to establish non-oxidizing conditions during experiments (it is not possible to control $fO_2$ at a specific value at the low temperatures of this study by mixing CO and $CO_2$). Experiments were terminated by dropping the samples in an actively cooled zone for fast quench.

## 3 Modeling of hydrogen diffusion

Diffusion profiles were fitted using an explicit numerical solution. Concentration changes with time at a specific location are described by Fick's second law (equation 1), with $c$ being the concentration, $t$ being time, $x$ being the distance, and $D$ being the diffusion coefficient. A finite difference scheme was used to solve the diffusion equation (equation 2), with $\Delta t$ being the time step size, $\Delta x$ being the distance step size, $c$ being

$$\frac{\partial c(x,t)}{\partial t} = D\frac{\partial^2 c(x,t)}{\partial x^2} \qquad (eq.1)$$

$$c_{i,j+1} = c_{i,j} + \frac{D\cdot\Delta t}{\Delta x^2}\cdot\left[c_{i+1,j} - 2c_{i,j} + c_{i-1,j}\right] \qquad (eq.2)$$

$$\sigma_{fit} = \frac{1}{N}\sqrt{\sum(c_{ms}(x) - c_{cal}(x))^2} \qquad (eq.3)$$

the concentration with the two subscripts $i$ and $j$ being indices for space and time, respectively. The geometry of the diffusion problem in this study involves a concentration gradient (i.e., implantation peak) that is located far from the crystal surface (Figure 2). Thus, the system boundaries are unaffected by diffusion (i.e., infinite medium) and are modelled to be open at both ends of each profile. The reader is referred to Costa *et al.* (2008) for a detailed description of the numerical solution. Notably, the non-destructive NRRA allows us to measure concentration profiles prior to experiments that are used as an initial condition (t = 0) in diffusion calculations (i.e., providing $c_{i,0}$ values). This approach provides an ideal description of the diffusion geometry, in contrast to an assumed initial profile (e.g., Gaussian). Finally, this

allows to model much smaller changes in hydrogen distribution, and it eliminates the necessity to consider convolution effects.

Diffusion of hydrogen at experimental temperatures led to a broadening of the implanted concentration peak while its maximum decreased. The resulting concentration profile could be satisfactorily fitted with a constant diffusion coefficient *D* along the profile distance at a given temperature, which indicates that there is no observable dependence of diffusion rates on

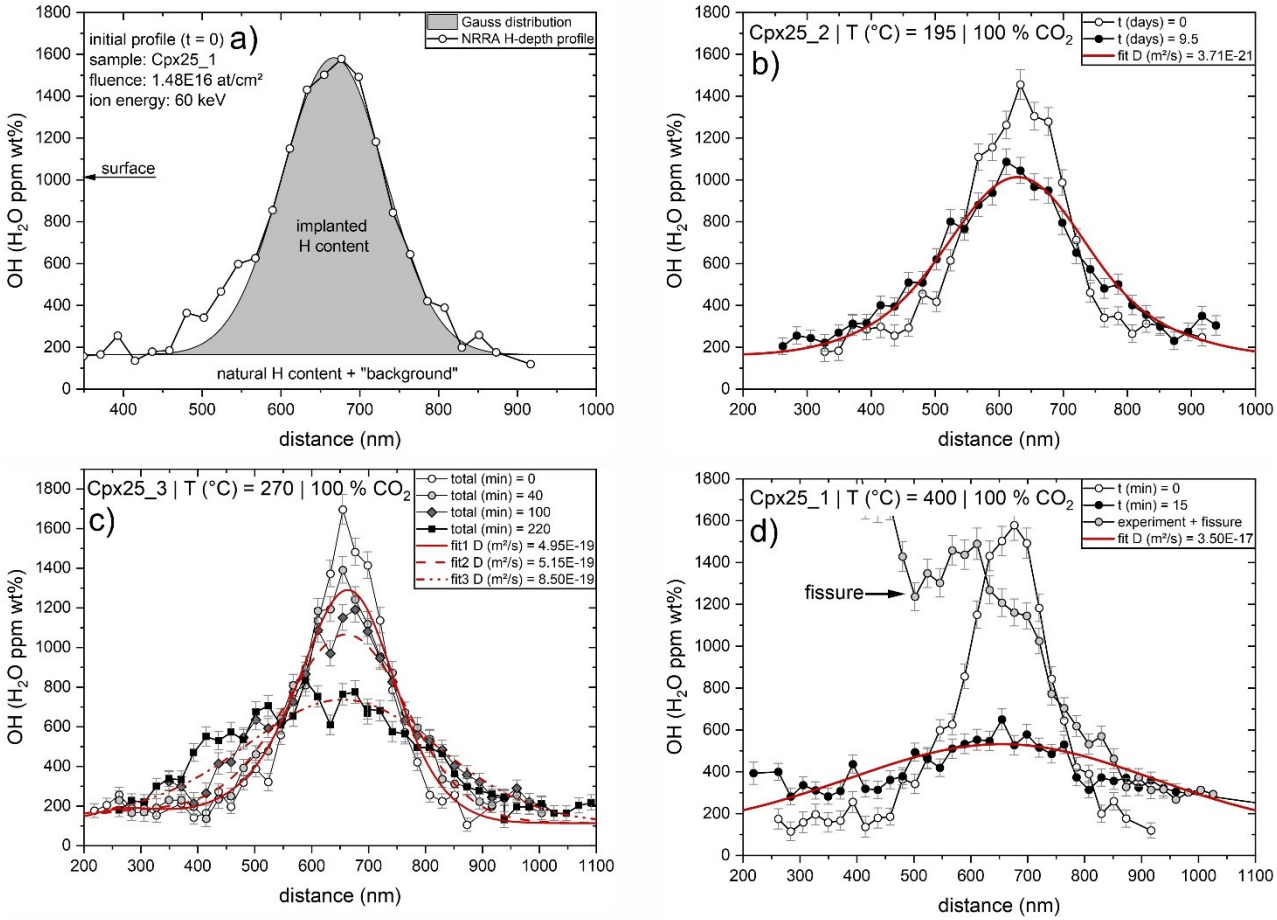


**Figure 2:** (a) Example for a hydrogen concentration depth profile produced by ion implantation and measured by NRRA (open circles). The shape of the peak can be described a Gaussian distribution (grey area). (b) The initial hydrogen implantation profile (open circles) broadened and flattened due to diffusion at 195 °C for 9.5 days (filled circles). The red line is the best fit of the numerical solution. (c) A time-series was performed in sample Cpx25_3 at 270 °C. The obtained diffusion coefficients from best fits display consistency over time. (d) The concentration profile in Cpx25_1 was strongly modified after only 15 minutes at 400 °C. The grey circles illustrate how a depth profile is affected if a fissure loaded with adsorbed atmospheric water interferes with NRRA analysis (i.e., the ion beam spot).

hydrogen concentration. Experiments were conducted at three different temperatures, 195 °C, 270 °C, and 400 °C (Figure 2b-c). A timeseries of 3 experiments within one sample (Cpx25_3) at 270 °C gives insight on how the diffusion profile develops within one sample with increasing

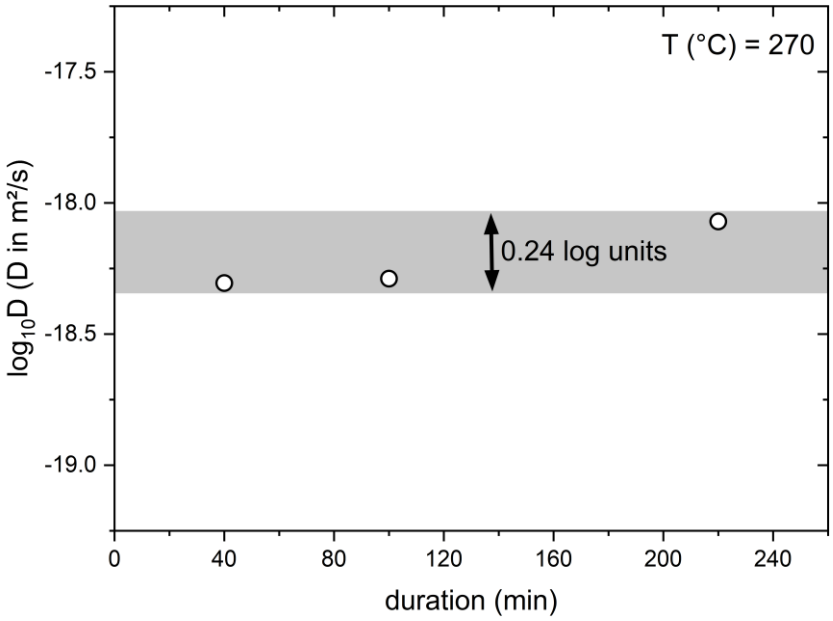


**Figure 3:** Diffusion coefficients that were obtained from fitting concentration profiles from the time-series at 270 °C yield constant values over time. The range of scatter in $\log_{10}D$ is about 0.24 log units and is larger than error estimates calculated from error propagation. For further details see Appendix A in Faak *et al.* (2013).

experimental duration. It was also used to assess the suitability of our method for obtaining diffusion coefficients, which is supported by almost constant diffusion coefficients ($\Delta \sim 0.24$ log units, Figure 3) in this time-series. D values were constrained by minimizing the misfit ($\sigma_{fit}$) between each measured concentration, $c_{ms}(x)$, and the corresponding calculated concentration, $c_{cal}(x)$ at the same location (equation 3). A summary of the experiments, determined diffusion coefficients, and misfit $\sigma_{fit}$ is provided in Table 1.

**Table 1:** Diffusion experiments at 195°C, 270 °C, and 400 °C. For the timeseries the total duration is the sum of the dwell time.

| Sample_experiment | T (°C) | Total duration | D (m²/s) | $\sigma_{fit}$ |
|---|---|---|---|---|
| Cpx25_1_EXP1 | 400 | 15 min | 3.50E-17 | 0.015 |
| Cpx25_2_EXP1 | 195 | 9.5 days | 3.71E-21 | 0.006 |
| Cpx25_3_EXP1 | 270 | 40 min | 4.95E-19 | 0.007 |
| Cpx25_3_EXP2 | 270 | 100 min | 5.15E-19 | 0.010 |
| Cpx25_3_EXP3 | 270 | 220 min | 8.50E-19 | 0.006 |

# 4 Comparison with previous studies

Diffusion rates that were determined in our experiments describe an Arrhenius relation $D_H = 5.47 (\pm 13.98) \cdot 10^{-8} \cdot exp (-115.64 (\pm 11.5)\ kJ\ mol^{-1} /RT)\ m^2 s^{-1}$ (purple solid line, Figure 4). Our experimental method allowed us to explore diffusion of hydrogen in diopside ($X_{Fe}$ = Fe/(Fe+Mg) = 0.102) at low temperatures (195 – 400 °C). However, a comparison of our results with those of other studies in clinopyroxene is restricted to higher temperatures (≥ 600 °C).

Ingrin *et al.* (1995) conducted dehydration experiments in Russian gem quality diopside ($X_{Fe}$ = 0.036) crystals at 700 to 1000 °C in air. They studied diffusion along three crystallographic directions, [001], [100]*, and [010] using FTIR but did not find anisotropy in diffusion rates. Thus, they propose that diffusion of hydrogen is isotropic in diopside. The temperature dependence, which is valid for all orientations, is expressed by an Arrhenius relation $D_H = 5.04 (\pm 14.12) \cdot 10^{-7} \cdot exp (-136 \pm 27\ kJ\ mol^{-1} /RT)\ m^2/s$ (grey solid line, Figure 4).

Instead of dehydration experiments, Hercule and Ingrin (1999) performed extraction-incorporation experiments in diopside crystals similar to those used in Ingrin *et al.* (1995) at 700 – 1000 °C at a $pH_2$ of 0.1 atm and 1 atm. Similar to Ingrin *et al.* (1995) they observe that the kinetics are independent of crystallographic orientation, but also of the partial pressure of $H_2$ and oxygen fugacity $fO_2$. They determined an Arrhenius law $D = 2.00 (\pm 5.05) \cdot 10^{-7} \cdot exp (-126 \pm 24\ kJ\ mol^{-1} /RT)\ m^2/s$ for this set of experiments (green dotted line, Figure 4). The authors also carried out hydrogen-deuterium exchange experiments in the same diopside at 600 – 900 °C along [001], [100]*, and [010] at 1 atm. They observe that diffusion along [001] and [100]* is two orders of magnitude faster than the incorporation rate from the other experimental setup. The Arrhenius relation is $D_H = 3.98 (\pm 7.33) \cdot 10^{-4} \cdot exp (-149 \pm 16\ kJ\ mol^{-1} /RT)\ m^2/s$ (green dashed line, Figure 4). Diffusion along [010] is slower than in the other directions but one magnitude faster than the H uptake. The related Arrhenius law is $D_H = 1.00 (\pm 3.91) \cdot 10^{-5} \cdot exp (-143 \pm 33\ kJ\ mol^{-1} /RT)\ m^2/s$ (green solid line, Figure 4). They conclude that incorporation of hydrogen is coupled to oxidation-reduction of iron $Fe^{3+} + O^{2-} + 1/2H_2\ (g) = Fe^{2+} + OH^-$. Hence, the rate of hydrogen uptake is a function of the crystals Fe-content (Hercule and Ingrin 1999).

Woods *et al.* (2000) used Jaipur diopside crystals ($X_{Fe}$ = 0.069) for dehydration experiments between 700 and 850 °C and at $fO_2$ of $10^{-14}$ bar. A comparison of diffusion rates between crystallographic orientations shows that rates along [100] and [001]* are fastest with the Arrhenius relations $D_H = 7.94\ (\pm 34.75) \cdot 10^{-3} \cdot exp\ (-181 \pm 38\ kJ\ mol^{-1}\ /RT)\ m^2/s$ (yellow dashed line, Figure 4) and $D_H = 3.98\ (\pm 14.67) \cdot 10^{-4} \cdot exp\ (-153 \pm 32\ kJ\ mol^{-1}\ /RT)\ m^2/s$ (yellow solid line, Figure 4), respectively. The relatively narrow experimental temperature range did not allow them to obtain a temperature-relation for diffusivity along [010]. However, their experiments indicate that diffusion along [010] is an order of magnitude slower than in the other two directions. The observed anisotropy agrees with the results from Hercule and Ingrin (1999). Woods *et al.* (2000) point out that mm-size diopside crystals will be affected by re-equilibration at temperatures as low as 800 °C.

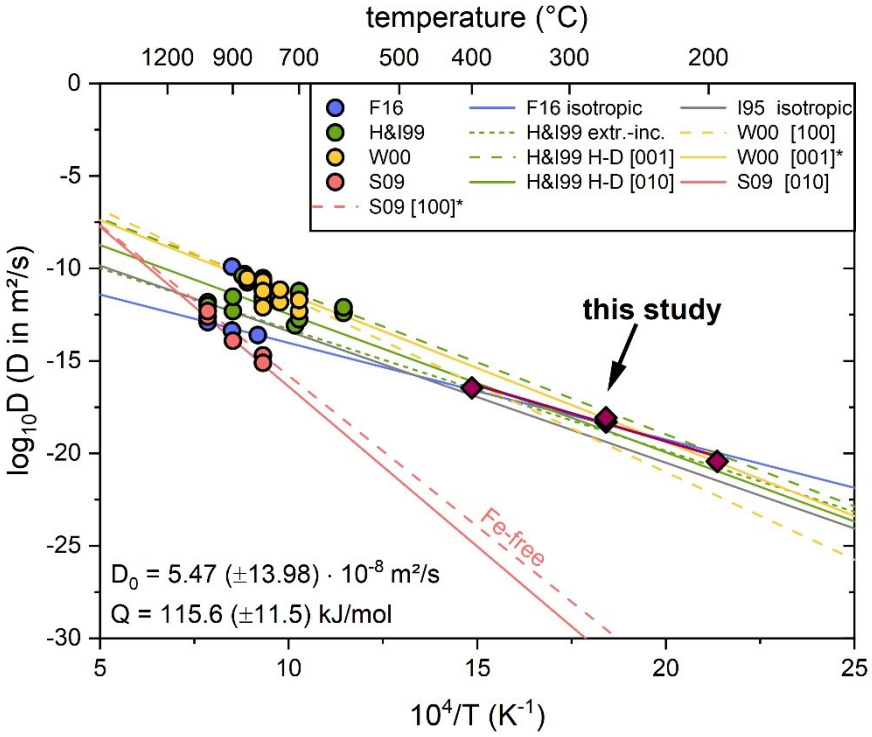


**Figure 4:** A comparison of published diffusion coefficients from high temperature experiments (T ≥ 600 °C) and associated Arrhenius relations (coloured lines) with results from this study (purple data, error bars smaller than symbols) confirm that latter lie well within the $\log_{10}$D range predicted by extrapolation from high temperatures. F16 = Ferriss et al. (2016); H&I99 = Hercule & Ingrin (1999); W00 = Woods et al. (2000); S09 = Sundvall et al. (2009); I95 = Ingrin et al. (1995).

Sundvall *et al.* (2009) used Fe-free diopside ($X_{Fe} \approx 0.0$) that was synthesized at water-saturated conditions. Their results from FTIR analysis of dehydration experiments at 800 – 1000 °C indicate that diffusion rates along [010] and [100]* are similar within error limits, which contradicts previous studies mentioned above. The Arrhenius relation for [010] is $D_H = 7.94 (\pm 42.07) \cdot exp (-331 \pm 50\ kJ\ mol^{-1}\ /RT)\ m^2/s$ (pink solid line, Figure 4). Diffusion rates along [100]* exhibit an Arrhenius relation $D_H = 3.16 (\pm 17.48) \cdot exp (-312 \pm 55\ kJ\ mol^{-1}\ /RT)\ m^2/s$ (pink dashed line, Figure 4). These diffusion rates are several orders of magnitude slower than in natural Fe-bearing samples. This difference also applies to diffusion rates we obtained in our natural diopside crystals when one extrapolates the high temperature data to low temperatures (pink lines, Figure 4).

Ferriss *et al.* (2016) studied dehydration in Kunlun diopside ($X_{Fe} = 0.025$), Jaipur diopside ($X_{Fe} = 0.075$), and augite ($X_{Fe} = 0.180$) at 800 – 1000 °C at an $fO_2$ at the QMF buffer. They present an Arrhenius relation for isotropic hydrogen diffusion in Kunlun diopside $D_H = 1.59 (\pm 31.02) \cdot 10^{-9} \cdot exp (-100.4 \pm 2.7\ kJ\ mol^{-1}\ /RT)\ m^2/s$ (blue solid line, Figure 4). Experiments in the Jaipur diopside and augite, which are more Fe-rich than the Kunlun diopside, show faster diffusion of hydrogen at the same temperature. This suggests that higher Fe contents cause faster diffusion rates of hydrogen. The authors also compare diffusion rates of hydrogen between clinopyroxenes of various Fe contents, including other studies. There is an increase in diffusion coefficients with increasing Fe-contents, but this increase diminishes towards high Fe contents. As pointed out by Ferriss *et al.* (2016), a compositional dependence of hydrogen diffusion in clinopyroxene might not be adequately described by the Fe content, instead Al could also play a significant role as has been shown for orthopyroxene by Kumamoto *et al.* (2019). Unfortunately, they do not provide Arrhenius relations for the Jaipur diopside and augite, which precludes a direct comparison of results from these samples with results of our study. However, an extrapolation of the Arrhenius law that was obtained for the Kunlun diopside is in excellent agreement with our results, although $X_{Fe}$ is much higher in our diopside (0.102 vs. 0.025). The conformity of diffusion rates in our diopside and the Kunlun diopside despite substantially different Fe contents ($X_{Fe}$ of our sample lies between that of the Jaipur diopside and augite) also indicates a more complex composition-diffusivity relationship.

A comparison of our diffusion rates with extrapolations from previous studies at high temperatures, highlights that we were able to resolve the outstanding issue whether diffusion rates can be extrapolated from high temperatures towards low temperatures. Our results lay well within the range that is constrained by extrapolation of Arrhenius relationships from high temperature experiments for Fe-bearing diopside to temperatures relevant in this study (Figure

4). Although, we did not constrain diffusion rates as a function of crystal orientation, previous studies (e.g., Woods *et al.* 2000; Hercule and Ingrin 1999) suggest that diffusion coefficients along [001] are greatest and like those along [100]. Therefore, it is evident that the high diffusivity of hydrogen (compared to other elements) in clinopyroxene extends continuously towards low temperatures.

Further, diffusion profiles in our experiments are well fitted by a simple (i.e., concentration-independent) numerical diffusion model (solving Fick's second law, equation 1) and diffusion rates as a function of temperature describe an Arrhenius relation. The consistency of our results resolves two concerns that might arise when implanted concentration distributions are to be used for diffusion studies. (i) Does the damage introduced by ion implantation affect diffusion? (ii) Is the implanted hydrogen bonded to the mineral matrix like "natural" hydrogen? First, hydrogen is a light element and therefore causes less damage during implantation compared to heavy elements at low energies (Zhang *et al.* 2009). Further evidence for a negligible damage of the sample is provided by results of diffusion experiments. Sample damaging (i.e., introduction of defects) due to irradiation follows a distribution similar to that of the hydrogen concentration. Thus, the region between the sample surface and the end of the implantation peak is affected by irradiation damage, but not so the rest of the sample at greater depth. If irradiation damage is thought to be intense enough to affect diffusion to a non-negligible extent, one would expect this to be reflected in an asymmetric development of the concentration profile, caused by a different diffusion rate and/or mechanism in the damaged zone compared to the pristine crystal. This was not observed in our diffusion profiles (Figure 2). Regarding (ii), IR-measurements of implanted hydrogen in olivine confirm that all the implanted hydrogen is present as OH, similar to the bonding state of natural hydrogen (Schaible and Baragiola 2014). In this work we assume that clinopyroxene behaves the same way. Hypothetically, a change from H or $H_2$ to OH during annealing in diffusion experiments would be expected to be accompanied by a change in diffusion rate with time as the proportions of different H-species change. However, time-series experiments feature a constant diffusion rate within uncertainties (Figure 3). Last, implanted hydrogen fluences of $1.48 \cdot 10^{16}$ at/cm² are relatively low (peak maximum ~ 1 at% H; 1650 wt. ppm $H_2O$) but close to natural concentrations in mantle pyroxenes (e.g., Warren and Hauri 2014).

# 5 Evaluation of re-equilibration of H in clinopyroxene at temperatures below 600 °C.

## 5.1 A non-isothermal diffusion model

The newly determined diffusion rates at low temperatures offer us the opportunity to model changes in hydrogen concentrations in clinopyroxene due to diffusion at conditions that are relevant for late-stage hydration and dehydration. Diffusive flux occurs when there is a cause i.e., chemical disequilibrium, caused, for example, in response to changes in temperature, pressure, oxygen fugacity ($fO_2$), the speciation of accompanying fluids, and solubility of hydrogen in clinopyroxene while a crystal of clinopyroxene ascends from the mantle to Earth's

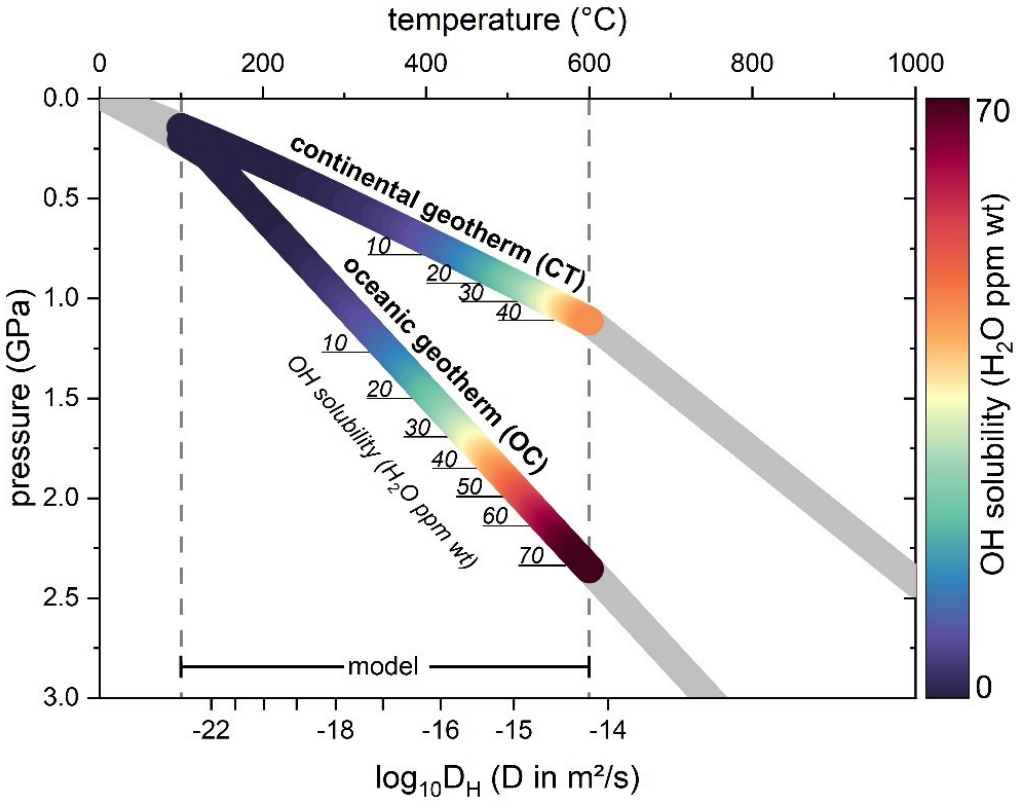


**Figure 5:** A continental geotherm (CT), an oceanic geotherm (OC), and solubilities of hydrogen in clinopyroxene that correspond to conditions along these PT paths (indicated by number labels and colour) were calculated following the procedure described in the Appendix. Diffusion rates in our model change during ascent according to the Arrhenius relationship obtained in this study (i.e., non-isothermal). Boundary concentrations that induce a concentration gradient change according to the solubility. Temperature boundaries of the model are indicated by dashed lines (600 °C to 100 °C).

surface, for example in volcanic rocks such as kimberlites or during the process of emplacement of an ophiolite. We have developed a model that simulates diffusion of hydrogen in clinopyroxene during its ascent, while the system variables change according to temperature-pressure paths and associated conditions (Figure 5).

Diffusion is calculated as a temperature dependent process (non-isothermal). The diffusion equation is solved using a finite difference model as described in section 3. The diffusion coefficient $D_H$ changes during the calculation according to the change in temperature during ascent and is derived from our Arrhenius relation $D_H = 5.47\ (\pm\ 13.98) \cdot 10^{-8} \cdot exp\ (-115.64\ (\pm 11.5)\ kJ\ mol^{-1}\ /RT)\ m^2 s^{-1}$. Possible effects of pressure and $fO_2$ on the diffusion coefficient are not included as they are expected to be weak but are not constrained experimentally. However, the variation of pressure and $fO_2$ in the surroundings plays an important role in the calculation through their influence on the boundary conditions. This is considered in our model (with $fO_2$ set to vary along the QMF buffer), as these variables control, together with temperature, the speciation of a C-O-H fluid (carbon saturated) that may be present. The associated $fH_2O$ affects the solubility of OH in clinopyroxene (Keppler and Bolfan-Casanova 2006). Boundary concentrations are adjusted to the appropriate values of hydrogen concentration at the rim corresponding to the P-T-$fO_2$ condition at each time step. The initial condition is taken to be a homogeneous hydrogen distribution in the crystal at equilibrium at the P-T-$fO_2$ condition of the starting depth.

The degree of re-equilibration was calculated using equation 4 where $c_{initial}$ is the initial concentration, $c_{model\ core}$ is the maximum concentration after cooling (usually in the core), and $c_{eq}$ corresponds to the final equilibrium concentration (i.e., the concentration at the rim of the crystal) (Chakraborty and Ganguly 1991; Costa *et al.* 2003; Lynn *et al.* 2017).

$$re - equilibration\ (\%) = \frac{c_{initial} - c_{model\ core}}{c_{initial} - c_{eq}} \times 100 \qquad (eq.4)$$

The results provide an impression of how the hydrogen budget and its distribution in clinopyroxene is modified and how this depends on the exhumation history and crystal size. We aim to clarify what the possibilities are in terms of hydrogen re-equilibration, demonstrated through some representative settings, rather than to reproduce and resolve specific cases. Therefore, two geotherms were calculated that are meant to constitute a continental (CT, 534

°C/GPa) and an oceanic (OC, 226 °C/GPa) setting. A detailed description of the development of this model is provided in Appendix I. Non-isothermal diffusion of hydrogen was modelled for clinopyroxene crystals of 2 mm, 1 mm, and 0.5 mm from 600 °C to 100 °C and the cooling rate (i.e., ascent rate) was varied by orders of magnitude (1000 to 0.1 °C/yr) to study its effect on the progress of equilibration. Figure 5 displays both geotherms in P-T-space whereas the modelled temperature range is indicated by dashed lines. The geotherm that reflects a continental lithosphere (CT) yields higher temperatures compared to the oceanic geotherm (OC) at same pressures, due to the assignment of higher radiogenic heat production to the former and a thin oceanic crust of 10 km to the latter (instead of 40 km, see Appendix I for more details).

Although diffusion rates that were derived from the experimentally established Arrhenius relationship are the same for both geotherms at similar temperature (D =f(T)), the pressure and therefore the solubility of OH in the model clinopyroxene is different. Consequently, the starting point at 600 °C corresponds to a higher pressure of 2.35 GPa for the oceanic and a lower pressure of 1.11 GPa for the continental model geotherm, which corresponds to 70.1 and 45.5 wt. ppm $H_2O$, respectively. This difference is reflected in the initial state of our models (t = 0) by a homogeneous concentration plateau and boundary concentrations at these values (Figure 6, dotted lines). A comparison of the evolution of hydrogen diffusion profiles in crystals of similar size that followed different P-T-paths reveals that at the same cooling rate the hydrogen content in the clinopyroxene that travelled along CT is more re-equilibrated than one that followed OC. This contrast is a consequence of different OH solubilities along the two paths that define the boundary concentrations (i.e., a compositional gradient), but not a result of different diffusivities. To further test the effect of solubility of OH on the progress of re-equilibration, we changed the boundaries to a fixed low concentration (= 0 wt. ppm) right from the start of diffusion until the final state is attained. We have done this for a cooling rate of 100°C/yr in 1 mm crystals along both geotherms (Figure 6, dashed lines). The obtained concentration profiles display an overall different shape compared to the original model that includes variable boundary concentrations. Steeper flanks towards the crystal surface are caused by a steep concentration gradient, which is present from the initial state, and which promotes a strong diffusive flux. Most notably, the extent of re-equilibration proceeded much more when the model did not include solubility-controlled boundary concentrations. Thus, a consideration

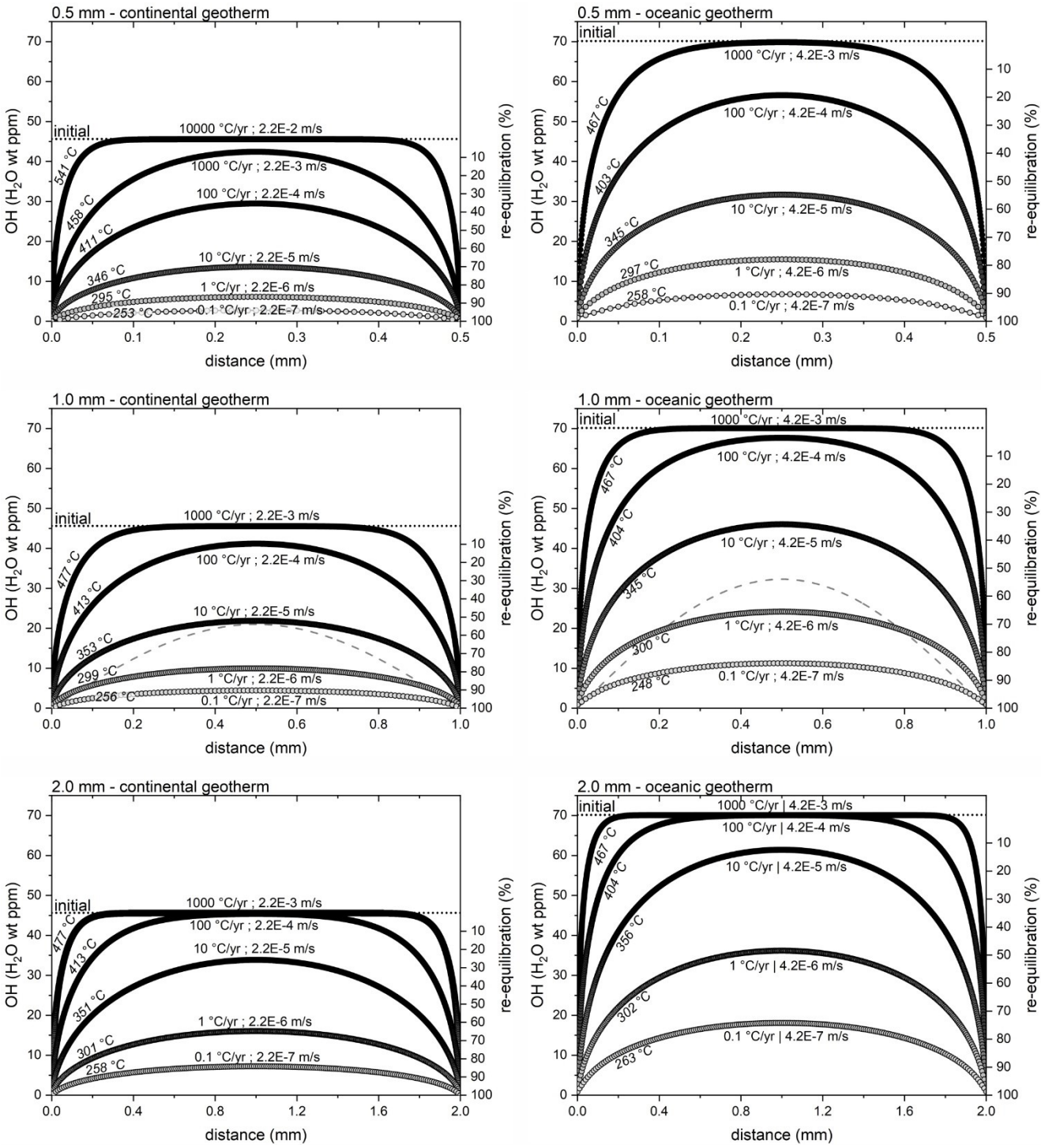


**Figure 6:** Diffusion profiles calculated from our model for the continental geotherm (CT, left side) and the oceanic geotherm (OC, right side) for crystal sizes of 0.5, 1.0, and 2.0 mm (top to bottom) using various cooling/ascent rates. The initial homogeneous OH concentration corresponds to the solubility of OH in clinopyroxene at the starting condition ($T_0$ = 600 °C and corresponding pressure) and is indicated by the dotted line (~46 wt. ppm for CT, ~70 wt. ppm for OC). Temperature labels below and above the profiles are apparent closure temperatures as a function of the cooling rate (taken from equilibrium temperatures corresponding to concentrations at 15 µm from the surface). The grey dashed lines in the 1.0 mm models are calculated concentration profiles for a cooling rate of 100 °C/yr, but the boundary concentrations were in this case set to the final concentration (at T = 100 °C) right from the beginning. The substantial differences in shape and extent of re-equilibration compared to the changing boundary concentration model emphasizes the influence of concentration gradients on the rate at which concentration profiles change.

of not only diffusivities, but of the system variables such as fluid composition (or, more generally, P-T-$fO_2$-$fH_2O$ conditions in the surrounding medium) that finally control OH solubility in the mineral is necessary to obtain trustworthy estimates on ascent rates or to assess the degree of re-equilibration. On the other hand, details of the profile shapes contain information on how the boundary conditions evolved with time – this may be helpful in setting the boundary conditions for modelling natural profiles.

### 5.2 Geological implications

Hydrogen concentration profiles that result from non-isothermal diffusion modelling illustrate that below some threshold in cooling rate for a given grain size the initial core concentration is no longer preserved. Small crystals at slow ascent rates show advanced re-equilibration, which is reflected by flat concentration profiles at low values (Figure 6). These should not be misinterpreted to be a sign for low water contents of the mantle, but to be results of a combination of relatively fast diffusion of hydrogen in clinopyroxene even at low temperatures and low H solubilities at those conditions. The dependence of re-equilibration on crystal size and cooling rate follows a systematic behaviour that can be described by equation 5 for each geotherm with the crystal size *sz* in mm, the cooling rate *cr* in °C/yr, and the fitting parameters *p1a*, *p1b*, *q1a*, *q1b*, *q2a*, and *q2b* (full description in Appendix II). This equation provides a tool to estimate the progress of re-equilibration for the range of crystal sizes and cooling rates for a given geotherm (Figure 7).

$$re-equilibration\ (\%) = \frac{p1a \times sz^{p1b}}{cr^2 + q1a \times sz^{q1b} \times cr + q2a \times sz^{q2b}} \qquad (eq.5)$$

These calculations have important geological implications, which we discuss below in the context of (1) ascent chronometry and (2) water contents in NAMs as signature of a mantle source.

(1) Fast diffusion of hydrogen in NAMs has been identified to be a promising tool to model ascent/decompression rates of magma (Newcombe *et al.* 2020) or to estimate eruption timescales in volcanic settings (Jollands *et al.* 2020). The principles of the method are that once an initial equilibrium water concentration was determined (either from water concentrations in

melt inclusions and $K_D$(NAM/melt) or directly from preserved hydrogen concentration plateaus in crystal cores) and concentration profiles that result from dehydration are measurable, diffusion modelling can be applied to constrain ascent rates. Our model indicates that even very small clinopyroxene crystal sizes (< 0.1 mm) potentially preserve original water contents at their cores at the lower boundary values for estimates on typical ascent rates in volcanoes (e.g., 0.05 MPa/s) and temperatures below 600 °C. This implies, that the hydrogen distribution that results from diffusion in NAMs that travel along an adiabat (as an approximation to transport

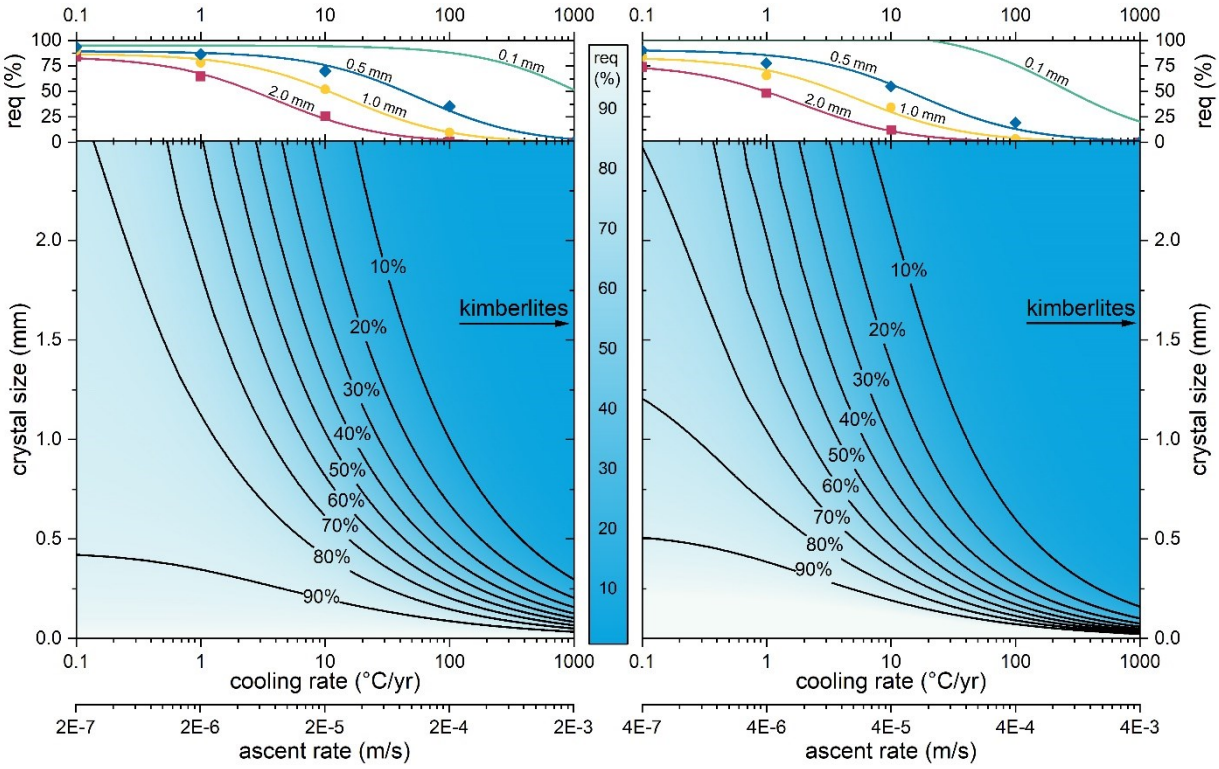


**Figure 7:** Re-equilibration (req) mapped as a function of crystal size and cooling rate/ascent rate for the continental geotherm (left) and the oceanic geotherm (right). Contours in both maps represent the extent of re-equilibration along these lines. The colour gradient visualizes the re-equilibration (blue = OH content preserved; white = completely re-equilibrated). The plotted lines at the top are re-equilibration profiles for 0.1 mm (green), 0.5 mm (blue), 1.0 mm (yellow), and 2.0 mm (pink) obtained from the model (equation 5). Symbols are the re-equilibration values calculated from the modelled diffusion profiles.

in a melt during ascent), are "frozen in" at relatively high temperatures (Figure 8, left). A modification of these at shallow depths are therefore less likely, and the measured profiles can be interpreted to record ascent rates at high temperatures. However, the uncertainty that is introduced by the choice of boundary concentrations that induce a concentration gradient can be very large. For example, a simplification of the problem to a scenario in which dehydration corresponds to a large concentration gradient from the beginning (e.g., 0 ppm) produces

overestimates on the order of an order of magnitude or so in cooling rates (see Figure 6, dashed lines in 1 mm profiles, Figure 8, right). Our model highlights that when changing boundary concentrations are applied, which are a better approximation to natural cases, the uncertainty in the determined cooling rates can be substantially reduced (Figure 8). Our model is set up for calculating ascent in any system (e.g., volcanoes or emplacement of massive lherzolites), but the boundary conditions in the model would need to be set according to the nature of the surrounding medium, and if it is not a C-O-H fluid then equation (5) would not apply (new calculations would be required to produce the equivalent of Eq. (5)).

(2) The finding that NAMs from mantle xenoliths contain hydrogen led to the conclusion that these contents represent hydrogen contents that are in equilibrium with a mantle source (Bell and Rossman 1992). Although NAMs incorporate only trace amounts of hydrogen, their major abundance in the mantle implies a large contribution to Earth's overall hydrogen budget and cycle. The effect hydrogen has on various properties of minerals (e.g., rheology and melting temperature) highlights the importance of carefully evaluating its abundance in mantle phases. Our results provide a basis to assess whether original hydrogen contents associated with a mantle source can be preserved during ascent or might be modified, or even completely erased. This helps to evaluate whether measured hydrogen concentrations in these natural samples can be interpreted as a mantle signature. Figure 7 shows that mantle xenoliths that were transported to the surface in a kimberlitic magma probably preserved the original hydrogen content due to the fast ascent rates (e.g., 5 – 37 m/s, Peslier *et al.* 2008). This means that OH concentrations that were measured for example by Bell and Rossman (1992) from a kimberlite source and by Peslier and Bizimis (2015) from Hawaiian peridotite probably reflect those of a mantle source. However, slow cooling or dwelling at temperatures that are typical for serpentinization (~ 300 °C, Guillot *et al.* 2015) can erase a mantle signature in large crystals (2 mm) in a few thousand years (Figure 9, left). Results from modelling hydrogen diffusion in clinopyroxene at 300 °C illustrate the development of the hydrogen distribution at temperatures associated with serpentinization, a process that was first suggested by Lynn and Warren (2021) and is supported by the newly obtained low-temperature diffusivity constraints here. As an example, after 2000 years at 300 °C, diffusion strongly modifies the distribution from rim to core, while the core content is almost preserved (dependent on the boundary concentration). Although, a mantle signature could have been preserved in the core, the result highlights the requirement for a careful analysis of core contents. Accurate measurements should prevent integration of

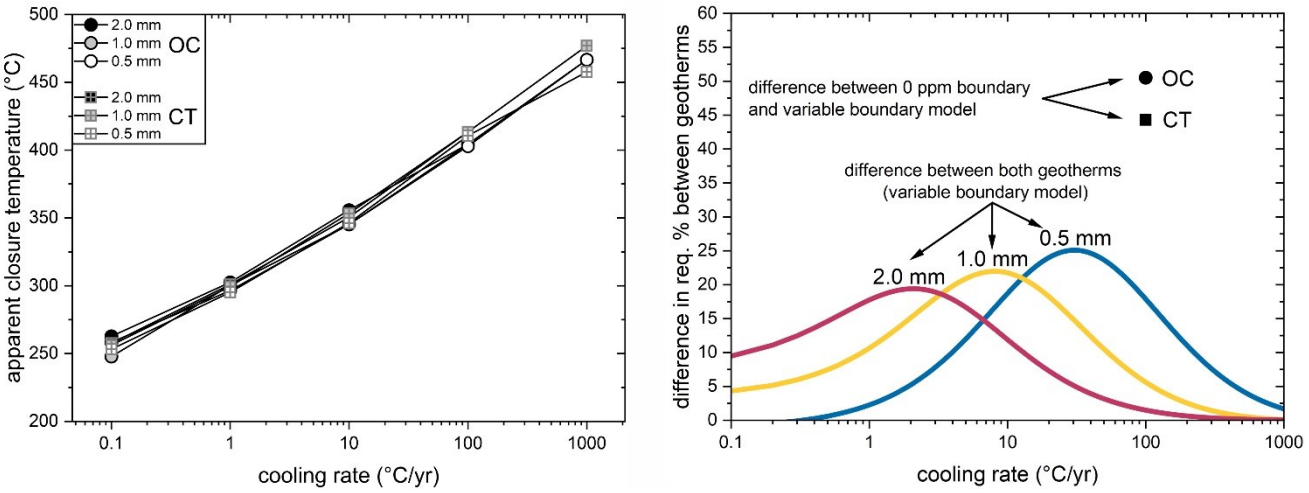


**Figure 8:** Left – freezing temperature as a function of cooling rate. Clinopyroxene crystals that were transported in a melt during ascent in volcanic settings are expected to experience fast cooling (> 1000 °C/yr) and therefore preserve a hydrogen distribution that was established at higher temperatures. Slow exhumation (i.e., slow cooling) allows the modification of hydrogen distribution within NAMs in response to lower equilibrium contents at the mineral boundary at low temperatures. Right – Differences in re-equilibration between the two geotherms for different crystal sizes and as a function of cooling rate (lines). In general, differences in the degree of re-equilibration between crystals of the same size but that travelled along different geotherms are smaller for larger crystals. However, this is complicated by a dependence on cooling rate. At low cooling rates larger crystals display greater differences in the degree of re-equilibration between both geotherms. Notably, setting the boundary concentration to a constant value of 0 ppm (instead of a variable boundary concentration) introduces large differences in the degree of re-equilibration (symbols).

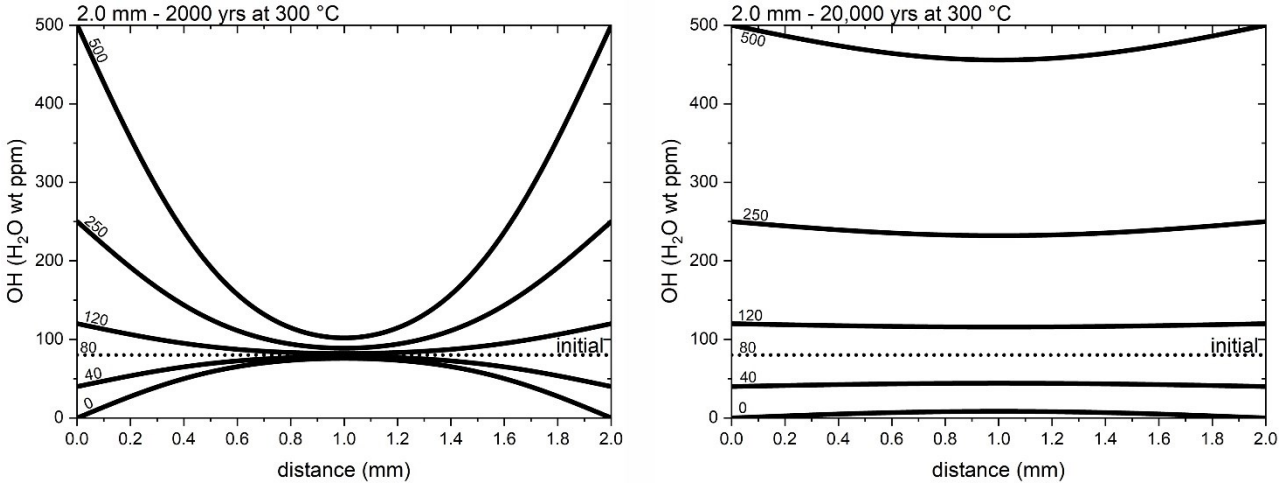


**Figure 9:** Modelling of isothermal diffusion at 300 °C for a 2 mm crystal with constant boundary concentrations that mimics dwelling at a temperature that is characteristic for serpentinization. The initial OH concentration (dotted line) is set to 80 OH ($H_2O$ wt ppm) Using different fixed boundary concentrations (numbers above and below profiles) highlight their influence on the progress of re-equilibration and change in profile shape. Left - Notably, the core concentration is in almost all cases preserved after 2,000 years although boundary concentrations are very high (e.g., 500 wt ppm). However, concentrations in the rim have substantially changed. Right - The original hydrogen content almost completely re-equilibrated to the boundary concentration after 20,000 years at 300 °C.

477 hydrogen contents from the either dehydrated or hydrated rim. Finally, after 20,000 years at

300 °C the original hydrogen concentration is almost completely homogenized (Figure 9, right); these effects are stronger in smaller crystals / diffusion domains (note that the distance to nearest source of hydration / dehydration, e.g. a crack, is relevant in this context rather than the size of a grain).

# 6 Conclusion

Diffusion experiments at low temperatures (195 - 400 °C) and non-isothermal modelling has resulted in the following conclusions:

(1) We applied an experimental and analytical procedure that enables us to study diffusion of hydrogen in clinopyroxene at low temperatures (≤ 400 °C). It was possible to circumvent previous hindrances by using ion implantation to introduce an artificial hydrogen concentration gradient. Concentration profiles on a nm-scale and changes in these due to diffusion at experimental temperatures were measured using Nuclear Resonance Reaction Analysis (NRRA). Taking advantage of the non-destructive nature of NRRA allowed us to observe the evolution of diffusion profiles with time within one sample, and thereby resolve small differences in concentration profile shapes before and after diffusion. Diffusivities are constant over time and show no concentration dependence. The diffusion-temperature relationship is described by an Arrhenius law $D_H = 5.47\ (\pm 13.98) \cdot 10^{-8}\ m^2/s \cdot exp\ [-115.6\ (\pm 11.5)\ kJ/mol/RT]$.

(2) A determination of diffusion coefficients for hydrogen in NAMs was possible only at high temperatures (> 600 °C) up to now. However, re-equilibration at shallow depths far from the mantle source would occur at lower temperatures. It was therefore crucial to experimentally verify whether diffusion rates from high temperatures follow an Arrhenius relation to lower temperatures. Our experimental results from experiments between 195 and 400 °C prove that diffusion coefficients of hydrogen in clinopyroxene can be extrapolated to low temperatures.

(3) Non-isothermal diffusion modelling using the newly obtained diffusion coefficients at low temperatures provides information on the degree of re-equilibration as a function of crystal size and cooling rate for a specific geotherm. We modelled the ascent of

clinopyroxene (0.5, 1.0, 2.0 mm) in a temperature range of 600 to 100 °C while the concentration boundaries are determined by the solubility of hydrogen in clinopyroxene at the respective P-T-$fO_2$ conditions. Small clinopyroxene crystals of 0.5 mm preserve original water contents at cooling rates > 1,000 – 10,000 °C/yr ($1 \cdot 10^{-3}$ – $1 \cdot 10^{-2}$ m/s). However, at slow cooling rates (< 10 °C/yr) hydrogen contents in even large crystals of 2.0 mm size get substantially modified, thus erasing the hydrogen content equilibrated at mantle depths.

**Acknowledgements** T. Bissbort thanks J. Primocerio for providing the EPMA data of clinopyroxene used in this study and C. Hirschle for Laue analysis for crystal orientation. He also thanks C. Beyer for his assistance in the lab. T. Bissbort expresses great gratitude for the operators and technical staff at the Dynamitron-Tandem-Laboratorium (RUBION). This research is funded by the DFG Project nos. BE 1307/5-1 and CH 166/20-1.

## Data Availability Statement

Programs used in this work are available in the Supplementary Material.

# Appendix I

### *Development of a non-isothermal diffusion model with variable system boundaries*

We modeled diffusion of hydrogen in clinopyroxene of different sizes during their ascent along two geotherms (oceanic and continental) in a low temperature range of 600°C to 100 °C in the presence of a C-O-H fluid that is carbon saturated. A calculation of OH concentration profiles that result from these scenarios required a derivation of parameters that affect diffusion, which is outlined in the following. A temperature-depth relationship was derived after Sclater *et al.* (1980), equations A1-A3 and Table A 1. The quantities in equation A1-A3 are explained in the table caption.

$$RHP = \frac{q_{surface} - q_{base}}{h_r} \qquad (eq.A1)$$

$$T_{crust} = T_0 + \frac{q_{base} z}{k_1} + \frac{(q_{surface} - q_{base}) \times h_r}{k_1}\left(1 - e^{-\frac{z}{h_r}}\right) \qquad (eq.A2)$$

$$T_{mantle} = T_{crust\_base} + \frac{(z - z_{crust})}{k_2} \times q_{base} \qquad (eq.A3)$$

**Table A 1***:* Parameters that were used to compute geotherms associated with an oceanic (OC) and a continental (CT) setting. $d_c$ = thickness of the crust, $\rho_c$ = density of the crust, $q_{surface}$ = surface heat flow, RHP = radiogenic heat production, $k_c$: thermal conductivity of the crust, $h_r$ = ratio of heat flow to heat production, $\rho_m$ = density of the mantle, $q_{base}$ = heat flow base of crust, $k_m$ = thermal conductivity mantle. 1 = Philpotts and Ague (2009), 2 = Carlson and Herrick (1990), 3 = Christensen and Mooney (1995), 4 = Sclater *et al.* (1980), 5 = Dziewonski and Anderson (1981).

| | crust | | | | | | mantle | | |
|---|---|---|---|---|---|---|---|---|---|
| **setting** | **$d_c$ (km)** | **$\rho_c$ (kg/m³)** | **$q_{surface}$ (mW/m²)** | **RHP (µW/cm³)** | **$k_c$ (W/K m)** | **$h_r$ (km)** | **$\rho_m$ (kg/m³)** | **$q_{base}$ (mW/m²)** | **$k_m$ (W/K m)** |
| **OC** | 10[1] | 2900[2] | 34[4] | 0.89 | 2.51[4] | 10 | 3380[5] | 25.1[4] | 3.35[4] |
| **CT** | 40[1] | 2830[3] | 46[4] | 1.20 | 2.51[4] | 10 | 3380[5] | 34.0[4] | 3.35[4] |

564 The lithostatic pressure along the geotherms was calculated by integrating the densities with
565 depth followed by multiplication with the constant for accelearation due to gravity. The oxygen
566 fugacity was assumed to be continuously buffered by a QMF assemblage. Whether hydration
567 or dehydration occurs also depends on the solubility of hydroxyl in clinopyroxene at respective
568 conditions and the availability of a hydrogen source (in this case a fluid). The solubility of
569 hydrogen in NAM is a function of pressure, temperature, and $fH_2O$, but is also affected by
570 contents of certain elements (e.g., Al) and $fO_2$ (Liu and Yang 2020). We used the solubility law,
571 equation A4, and experimentally determined values by Liu and Yang (2020) and Bromiley *et*
572 *al.* (2004) ($dH$ = 21.2 kJ/mol, $dV$ = 7.3 cm³/mol, $A$ = 7.144 ppm/bar, $n$ = 0.5) to describe
573 solubility of hydroxyl ($c_{water}$ in wt. ppm $H_2O$) in clinopyroxene as a function of temperature,
574 pressure, and $H_2O$ fugacity ($fH_2O$). The latter is controlled by the speciation of the present fluid,
575 which was determined from thermodynamic modelling of a C-O-H (carbon saturated and fixed
576 $fO_2$ at QMF) fluid as a function of temperature, pressure, and $fO_2$ following the procedure in
577 Huizenga (2005). The database of fugacity coefficients of the species used in Huizenga (2005)
578 had to be extended by extrapolation in P-T space (between 100 °C and 300 °C), which is a
579 sufficient approximation for our purpose. OH contents that were derived from the solubility law
580 were used as boundary concentrations that were constantly changing (i.e., decreasing) and
581 thereby introducing a concentration gradient at the system boundaries.
582

583 $$c_{water} = A f H_2O^n \exp\left(-\frac{dH^{1bar} + dV^{solid} P}{RT}\right) \qquad (eq.A4)$$

584

585 In the final model, the rate of diffusion is affected by changes in temperature and was thus
586 computed as non-isothermal process by allowing the diffusion coefficient to change according
587 to the respective temperature. The diffusion coefficients were derived through the Arrhenius
588 relationship $D_H = 5.47\ (\pm 13.98) \cdot 10^{-8}\ m^2/s \cdot exp\ [-115.6\ (\pm 11.5)\ kJ/mol/RT]$ which was obtained
589 through our experiments. Effects of pressure and $fO_2$ on hydrogen diffusion in clinopyroxene
590 are experimentally weakly or not constrained but are expected to play a minor role compared
591 to temperature. The actual diffusion modelling was performed by approximating Fick's second
592 law (equation A5) by an explicit numerical solution (finite difference, equation A6).

593

594 $$\frac{\partial c(x,t)}{\partial t} = D \frac{\partial^2 c(x,t)}{\partial x^2} \qquad (eq.A5)$$

595

596 $$c_{i,j+1} = c_{i,j} + \frac{D \cdot \Delta t}{\Delta x^2} \cdot \left[c_{i+1,j} - 2c_{i,j} + c_{i-1,j}\right] \quad (eq.A6)$$

597

598 The initial condition (t = 0) for the diffusion model is a homogeneous hydrogen distribution in
599 the crystal. This initial concentration corresponds to the solubility of *OH* in clinopyroxene at
600 the starting P-T-$fH_2O$ condition. During the diffusion calculation the diffusion rate $D_H$ is
601 continuously changed according to the temperature at that time step. All codes that were used
602 in these calculations are provided in the Supplementary Material.

603

604

605

606

607

608

609

610

611

612

613

614

615

616

617

618

619

620

621

622

623

624

# Appendix II

### *Fitting re-equilibration as a function of crystal size and cooling rate*

Re-equilibration is defined by equation A7 with $c_{initial}$ being the initial *OH* concentration (t = 0), $c_{model\ core}$ being the *OH* concentration in the crystal core after diffusion, $c_{equilibrium\ at\ T(final)}$ being the equilibrium concentration at the final temperature (here 100 °C). The degree of re-equilibration is calculated for each crystal size, cooling rate, and geotherm. The re-equilibration – cooling rate relationship (Figure S1 and S2 in supplementary information) is then fitted using equation A8 to obtain parameters *p1*, *q1*, *q2* for each geotherm and crystal size. *MATLAB curve fitting* tool and the implemented non-linear least square procedure (Levenberg-Marquardt algorithm) was used for all fitting procedures that are described in this chapter.

$$re-equilibration\ (\%) = \frac{c_{initial} - c_{model\ core}}{c_{initial} - c_{equilibrium\ at\ T(final)}} \times 100 \qquad (eq.A7)$$

$$re-equilibration\ (\%) = \frac{p1}{cr^2 + q1 \times cr + q2} \qquad (eq.A8)$$

**Table A 2:** Parameters *p1*, *q1*, *q2* obtained by fitting re-equilibration – cooling rate relationships for each crystal size and geotherm.

| Geotherm / crystal size | p1 | q1 | q2 | $R^2$ |
|---|---|---|---|---|
| CT / 0.5 mm | 9.972E+6 | 1.955E+3 | 1.118E+5 | 0.9826 |
| CT / 1.0 mm | 9.492E+5 | 7.668E+2 | 1.081E+4 | 0.9955 |
| CT / 2.0 mm | 8.962E+4 | 2.665E+2 | 1.060E+3 | 0.9958 |
| OC / 0.5 mm | 1.889E+10 | 1.307E+7 | 2.067E+8 | 0.9668 |
| OC / 1.0 mm | 4.902E+5 | 9.293E+2 | 6.008E+3 | 0.9899 |
| OC / 2.0 mm | 9.555E+4 | 7.263E+2 | 1.220E+3 | 0.9990 |

The fitting parameters *p1*, *q1*, and *q2* were then fitted as a function of crystal size for both geotherms using simple power-law equations (eq. A9-A11).

$$p1 = p1a \times sz^{p1b} \qquad (eq.A9)$$

$$q1 = q1a \times sz^{q1b} \qquad (eq.A10)$$

$$q2 = q2a \times sz^{q2b} \qquad (eq.A11)$$

**Table A 3:** Parameters obtained by fitting re-equilibration as a function of crystal size (sz) and cooling rate (cr) for the two geotherms CT and OC.

| **parameter** | **CT** | **OC** |
|---|---|---|
| p1a | 9.4663E+5 | 9.6171E+6 |
| p1b | -3.399 | -8.8003 |
| $R^2$ | 1.00 | 1.00 |
| q1a | 7.3650E+2 | 2.0662E+4 |
| q1b | -1.4375 | -7.0677 |
| $R^2$ | 0.99 | 1.00 |
| q2a | 1.0861E+4 | 1.1485E+5 |
| q2b | -3.3604 | -8.6851 |
| $R^2$ | 1.00 | 1.00 |

Substituting parameters *p1*, *q1*, and *q2* in equation A8 by the power-law equations A9-A11 above yields the following equation A12 that was used to calculate re-equilibration in % as a function of crystal size *sz* in mm and cooling rate *cr* in °C/yr for both geotherms.

$$re-equilibration\ (\%) = \frac{p1a \times sz^{p1b}}{cr^2 + q1a \times sz^{q1b} \times cr + q2a \times sz^{q2b}} \qquad (eq.A12)$$

## References

**Becker, H. W.; Bahr, M.; Berheide, M.; Borucki, L.; Buschmann, M.; Rolfs, C.** *et al.* (**1995**): Hydrogen depth profiling using18O ions. In: *Z. Physik A - Hadrons and Nuclei* 351, 4, S. 453–465. DOI: 10.1007/BF01291151.

**Becker, H.-W.; Rogalla, D.** (**2016**): Nuclear Reaction Analysis. In: H. Fritzsche, J. Huot und D. Fruchart (Hg.): Neutron scattering and other nuclear techniques for hydrogen in materials. Cham: Springer (Neutron scattering applications and techniques), S. 315–336.

**Bell, D. R.; Rossman, G. R.** (**1992**): Water in Earth's Mantle: The Role of Nominally Anhydrous Minerals. In: *Science (New York, N.Y.)* 255, 5050, S. 1391–1397. DOI: 10.1126/science.255.5050.1391.

**Bissbort, T.; Becker, H.-W.; Fanara, S.; Chakraborty, S.** (**2021**): Novel approach to study diffusion of hydrogen bearing species in silicate glasses at low temperatures. In: *Chemical Geology* 562, S. 120037. DOI: 10.1016/j.chemgeo.2020.120037.

**Bromiley, G. D.; Keppler, H.; McCammon, C.; Bromiley, F. A.; Jacobsen, S. D.** (**2004**): Hydrogen solubility and speciation in natural, gem-quality chromian diopside. In: *American Mineralogist* 89, 7, S. 941–949. DOI: 10.2138/am-2004-0703.

**Carlson, R. L.; Herrick, C. N.** (**1990**): Densities and porosities in the oceanic crust and their variations with depth and age. In: *J. Geophys. Res.* 95, B6, S. 9153. DOI: 10.1029/JB095iB06p09153.

**Chakraborty, S.; Ganguly, J.** (**1991**): Compositional Zoning and Cation Diffusion in Garnets. In: Diffusion, Atomic Ordering, and Mass Transport: Springer, New York, NY, S. 120–175. Online verfügbar unter https://link.springer.com/chapter/10.1007/978-1-4613-9019-0_4.

**Chen, S.; Hiraga, T.; Kohlstedt, D. L.** (**2006**): Water weakening of clinopyroxene in the dislocation creep regime. In: *J. Geophys. Res.* 111, B8. DOI: 10.1029/2005JB003885.

**Christensen, N. I.; Mooney, W. D.** (**1995**): Seismic velocity structure and composition of the continental crust: A global view. In: *J. Geophys. Res.* 100, B6, S. 9761–9788. DOI: 10.1029/95JB00259.

**Costa, F.; Chakraborty, S.; Dohmen, R.** (**2003**): Diffusion coupling between trace and major elements and a model for calculation of magma residence times using plagioclase. In: *Geochimica et Cosmochimica Acta* 67, 12, S. 2189–2200. DOI: 10.1016/S0016-7037(02)01345-5.

**Costa, F.; Dohmen, R.; Chakraborty, S.** (**2008**): Time Scales of Magmatic Processes from Modeling the Zoning Patterns of Crystals. In: *Reviews in Mineralogy and Geochemistry* 69, 1, S. 545–594. DOI: 10.2138/rmg.2008.69.14.

**Demers-Roberge, A.; Jollands, M. C.; Tollan, P.; Müntener, O.** (**2021**): H diffusion in orthopyroxene and the retention of mantle water signatures. In: *Geochimica et Cosmochimica Acta* 305, S. 263–281. DOI: 10.1016/j.gca.2021.04.005.

**Demouchy, S.; Mackwell, S.** (**2006**): Mechanisms of hydrogen incorporation and diffusion in iron-bearing olivine. In: *Physics and Chemistry of Minerals* 33, 5, S. 347–355. DOI: 10.1007/s00269-006-0081-2.

**Demouchy, S.; Thoraval, C.; Bolfan-Casanova, N.; Manthilake, G. (2016)**: Diffusivity of hydrogen in iron-bearing olivine at 3GPa. In: *Physics of the Earth and Planetary Interiors* 260, S. 1–13. DOI: 10.1016/j.pepi.2016.08.005.

**Droop, G. T. R. (1987)**: A general equation for estimating Fe 3+ concentrations in ferromagnesian silicates and oxides from microprobe analyses, using stoichiometric criteria. In: *Mineral. mag.* 51, 361, S. 431–435. DOI: 10.1180/minmag.1987.051.361.10.

**Dziewonski, A. M.; Anderson, D. L. (1981)**: Preliminary reference Earth model. In: *Physics of the Earth and Planetary Interiors* 25, 4, S. 297–356. DOI: 10.1016/0031-9201(81)90046-7.

**Fei, H.; Druzhbin, D.; Katsura, T. (2020)**: The Effect of Water on Ionic Conductivity in Olivine. In: *J. Geophys. Res. Solid Earth* 125, 3. DOI: 10.1029/2019JB019313.

**Ferriss, E.; Plank, T.; Newcombe, M.; Walker, D.; Hauri, E. (2018)**: Rates of dehydration of olivines from San Carlos and Kilauea Iki. In: *Geochimica et Cosmochimica Acta* 242, S. 165–190. DOI: 10.1016/j.gca.2018.08.050.

**Ferriss, E.; Plank, T.; Walker, D. (2016)**: Site-specific hydrogen diffusion rates during clinopyroxene dehydration. In: *Contributions to Mineralogy and Petrology* 171, 6, S. 55. DOI: 10.1007/s00410-016-1262-8.

**Gose, J.; Schmädicke, E.; Stalder, R. (2011)**: Water in mantle orthopyroxene – no visible change in defect water during serpentinization. In: *Eur.J.Mineral.* 23, 4, S. 529–536. DOI: 10.1127/0935-1221/2011/0023-2122.

**Guillot, S.; Schwartz, S.; Reynard, B.; Agard, P.; Prigent, C. (2015)**: Tectonic significance of serpentinites. In: *Tectonophysics* 646, S. 1–19. DOI: 10.1016/j.tecto.2015.01.020.

**Hercule, S.; Ingrin, J. (1999)**: Hydrogen in diopside; diffusion, kinetics of extraction-incorporation, and solubility. In: *American Mineralogist* 84, 10, S. 1577–1587. DOI: 10.2138/am-1999-1011.

**Hirschmann, M. (2006)**: Water, Melting, and the Deep Earth H2O Cycle. In: Annual Review of Earth and Planetary Sciences, 34:1, S. 629–653.

**Hirschmann, M.; Kohlstedt, D. L. (2012)**: Water in Earth's mantle. In: *Phys. Today,* 65.

**Hirth, G.; Kohlstedt, D. L. (1996)**: Water in the oceanic upper mantle: implications for rheology, melt extraction and the evolution of the lithosphere. In: *Earth and Planetary Science Letters* 144, 1-2, S. 93–108. DOI: 10.1016/0012-821X(96)00154-9.

**Huizenga, J. M. (2005)**: COH, an Excel spreadsheet for composition calculations in the C–O–H fluid system. In: *Computers & Geosciences* 31, 6, S. 797–800. DOI: 10.1016/j.cageo.2005.03.003.

**Ingrin, J.; Hercule, S.; Charton, T. (1995)**: Diffusion of hydrogen in diopside: Results of dehydration experiments. In: *J. Geophys. Res.* 100, B8, S. 15489–15499. DOI: 10.1029/95JB00754.

**Jollands, M. C.; Ellis, B.; Tollan, P. M.E.; Müntener, O. (2020)**: An eruption chronometer based on experimentally determined H-Li and H-Na diffusion in quartz applied to the Bishop Tuff. In: *Earth and Planetary Science Letters* 551, S. 116560. DOI: 10.1016/j.epsl.2020.116560.

**Jollands, M. C.; O'Neill, H. St.C.; Berry, A. J.; Le Losq, C.; Rivard, C.; Hermann, J. (2021)**: A combined Fourier transform infrared and Cr K-edge X-ray absorption near-edge structure spectroscopy study of the substitution and diffusion of H in Cr-doped forsterite. In: *Eur.J.Mineral.* 33, 1, S. 113–138. DOI: 10.5194/ejm-33-113-2021.

**Karato, S. (1990)**: The role of hydrogen in the electrical conductivity of the upper mantle. In: *Nature* 347, 6290, S. 272–273. DOI: 10.1038/347272a0.

**Karato, S.; Jung, H. (1998)**: Water, partial melting and the origin of the seismic low velocity and high attenuation zone in the upper mantle. In: *Earth and Planetary Science Letters* 157, 3-4, S. 193–207. DOI: 10.1016/S0012-821X(98)00034-X.

**Keppler, H.; Bolfan-Casanova, N. (2006)**: Thermodynamics of Water Solubility and Partitioning. In: *Reviews in Mineralogy and Geochemistry* 62, 1, S. 193–230. DOI: 10.2138/rmg.2006.62.9.

**Keppler, H.; Smyth, J. R. (2006)**: Water in Nominally Anhydrous Minerals. Berlin: De Gruyter (Reviews in Mineralogy & Geochemistry, 62).

**Kilgore, M. L.; Peslier, A. H.; Brandon, A. D.; Schaffer, L. A.; Morris, R. V.; Graff, T. G.** *et al.* **(2020)**: Metasomatic control of hydrogen contents in the layered cratonic mantle lithosphere sampled by Lac de Gras xenoliths in the central Slave craton, Canada. In: *Geochimica et Cosmochimica Acta* 286, S. 29–53. DOI: 10.1016/j.gca.2020.07.013.

**Kumamoto, K. M.; Warren, J. M.; Hauri, E. H. (2019)**: Evolution of the Josephine Peridotite Shear Zones: 1. Compositional Variation and Shear Initiation. In: *Geochemistry, Geophysics, Geosystems* 20, 12, S. 5765–5785. DOI: 10.1029/2019GC008399.

**Le Roux, V.; Urann, B. M.; Brunelli, D.; Bonatti, E.; Cipriani, A.; Demouchy, S.; Monteleone, B. D. (2021)**: Postmelting hydrogen enrichment in the oceanic lithosphere. In: *Sci. Adv.* 7, 24, eabf6071. DOI: 10.1126/sciadv.abf6071.

**Liu, H.; Yang, X. (2020)**: Solubility of hydroxyl groups in pyroxenes: Effect of oxygen fugacity at 0.2–3 GPa and 800–1200 °C. Geochimica et Cosmochimica Acta, 286, 355-379. In: *Geochimica et Cosmochimica Acta* 286, S. 355–379. DOI: 10.1016/J.GCA.2020.07.034.

**Lynn, K. J.; Shea, T.; Garcia, M. O. (2017)**: Nickel variability in Hawaiian olivine: Evaluating the relative contributions from mantle and crustal processes. In: *msam* 102, 3, S. 507–518. DOI: 10.2138/am-2017-5763.

**Lynn, K. J.; Warren, J. M. (2021)**: The potential for aqueous fluid-rock and silicate melt-rock interactions to re-equilibrate hydrogen in peridotite nominally anhydrous minerals. In: *American Mineralogist. DOI:* 10.2138/am-2021-7435.

**Mackwell, S. J.; Kohlstedt, D. L. (1990)**: Diffusion of hydrogen in olivine: Implications for water in the mantle. In: *J. Geophys. Res.* 95, B4, S. 5079. DOI: 10.1029/JB095iB04p05079.

**Martin, R. F.; Donnay, G. (1972)**: Hydroxyl in the mantle. In: *American Mineralogist* 57, 3-4_Part_1, S. 554–570.

**Maurel, B.; Amsel, G. (1983)**: A new measurement of the 429 keV 15N(p,ay)12C resonance. Applications of the very narrow width found to 15N and 1H depth location. In: *Nuclear Instruments and Methods in Physics Research* 218, 1-3, S. 159–164. DOI: 10.1016/0167-5087(83)90973-0.

**Moine, B. N.; Bolfan-Casanova, N.; Radu, I. B.; Ionov, D. A.; Costin, G.; Korsakov, A. V.** *et al.* (**2020**): Molecular hydrogen in minerals as a clue to interpret ∂D variations in the mantle. In: *Nat Commun* 11, 1, S. 3604. DOI: 10.1038/s41467-020-17442-8.

**Newcombe, M. E.; Plank, T.; Barth, A.; Asimow, P. D.; Hauri, E.** (**2020**): Water-in-olivine magma ascent chronometry: Every crystal is a clock. In: *Journal of Volcanology and Geothermal Research* 398, S. 106872. DOI: 10.1016/j.jvolgeores.2020.106872.

**Ohtani, E.; Litasov, K. D.** (**2006**): The Effect of Water on Mantle Phase Transitions. In: *Reviews in Mineralogy and Geochemistry* 62, 1, S. 397–420. DOI: 10.2138/rmg.2006.62.17.

**Osipowicz, T.; Lieb, K. P.; Brüssermann, S.** (**1987**). In: *Nuclear instruments and methods*.

**Padrón-Navarta, J. A.; Hermann, J.; St. O'Neill, H. C.** (**2014**): Site-specific hydrogen diffusion rates in forsterite. In: *Earth and Planetary Science Letters* 392, S. 100–112. DOI: 10.1016/j.epsl.2014.01.055.

**Peslier, A. H.; Bizimis, M.** (**2015**): Water in Hawaiian peridotite minerals: A case for a dry metasomatized oceanic mantle lithosphere. In: *Geochem. Geophys. Geosyst.* 16, 4, S. 1211–1232. DOI: 10.1002/2015GC005780.

**Peslier, A. H.; Bizimis, M.; Matney, M.** (**2015**): Water disequilibrium in olivines from Hawaiian peridotites: Recent metasomatism, H diffusion and magma ascent rates. In: *Geochimica et Cosmochimica Acta* 154, S. 98–117. DOI: 10.1016/j.gca.2015.01.030.

**Peslier, A. H.; Woodland, A. B.; Wolff, J. A.** (**2008**): Fast kimberlite ascent rates estimated from hydrogen diffusion profiles in xenolithic mantle olivines from southern Africa. In: *Geochimica et Cosmochimica Acta* 72, 11, S. 2711–2722. DOI: 10.1016/j.gca.2008.03.019.

**Philpotts, A.; Ague, J.** (**2009**): Principles of Igneous and Metamorphic Petrology. Cambridge: Cambridge University Press.

**Reynes, J.; Jollands, M.; Hermann, J.; Ireland, T.** (**2018**): Experimental constraints on hydrogen diffusion in garnet. In: *Contributions to Mineralogy and Petrology* 173, 9. DOI: 10.1007/s00410-018-1492-z.

**Schaible, M. J.; Baragiola, R. A.** (**2014**): Hydrogen implantation in silicates: The role of solar wind in SiOH bond formation on the surfaces of airless bodies in space. In: *J. Geophys. Res. Planets* 119, 9, S. 2017–2028. DOI: 10.1002/2014JE004650.

**Sclater, J. G.; Jaupart, C.; Galson, D.** (**1980**): The heat flow through oceanic and continental crust and the heat loss of the Earth. In: *Rev. Geophys.* 18, 1, S. 269. DOI: 10.1029/RG018i001p00269.

**Stalder, R.; Behrens, H.** (**2006**): D/H exchange in pure and Cr-doped enstatite: implications for hydrogen diffusivity. In: *Physics and Chemistry of Minerals* 33, 8-9, S. 601–611. DOI: 10.1007/s00269-006-0112-z.

**Stalder, R.; Skogby, H.** (**2003**): Hydrogen diffusion in natural and synthetic orthopyroxene. In: *Physics and Chemistry of Minerals* 30, 1, S. 12–19. DOI: 10.1007/s00269-002-0285-z.

**Sundvall, R.; Skogby, H.; Stalder, R.** (**2009**): Hydrogen diffusion in synthetic Fe-free diopside. In: *Eur.J.Mineral.* 21, 5, S. 963–970. DOI: 10.1127/0935-1221/2009/0021-1971.

**Tang, W.; Hui, H.; Ionov, D. A.; Chen, W.; Zhang, L.; Xu, Y.** (**2020**): Metasomatism-controlled hydrogen distribution in the Spitsbergen upper mantle. In: *msam* 105, 9, S. 1326–1341. DOI: 10.2138/am-2020-7290.

**Thoraval, C.; Demouchy, S.; Padrón-Navarta, J. A.** (**2019**): Relative diffusivities of hydrous defects from a partially dehydrated natural olivine. In: *Physics and Chemistry of Minerals* 46, 1, S. 1–13. DOI: 10.1007/s00269-018-0982-x.

**Tollan, P. M. E.; Smith, R.; O'Neill, H. St.C.; Hermann, J.** (**2017**): The responses of the four main substitution mechanisms of H in olivine to H2O activity at 1050 °C and 3 GPa. In: *Prog. in Earth and Planet. Sci.* 4, 1. DOI: 10.1186/s40645-017-0128-7.

**Wang, Y.-F.; Qin, J.-Y.; Soustelle, V.; Zhang, J.-F.; Xu, H.-J.** (**2021**): Pyroxene does not always preserve its source hydrogen concentration: Clues from some peridotite xenoliths. In: *Geochimica et Cosmochimica Acta* 292, S. 382–408. DOI: 10.1016/j.gca.2020.10.003.

**Warren, J. M.; Hauri, E. H.** (**2014**): Pyroxenes as tracers of mantle water variations. In: *J. Geophys. Res. Solid Earth* 119, 3, S. 1851–1881. DOI: 10.1002/2013JB010328.

**Woods, S. C.; Mackwell, S.; Dyar, D.** (**2000**): Hydrogen in diopside. Diffusion profiles. In: *American Mineralogist* 85, 3-4, S. 480–487. DOI: 10.2138/am-2000-0409.

**Zhang, Y.; Bae, I.-T.; Sun, K.; Wang, C.; Ishimaru, M.; Zhu, Z.** *et al.* (**2009**): Damage profile and ion distribution of slow heavy ions in compounds. In: *Journal of Applied Physics* 105, 10, S. 104901. DOI: 10.1063/1.3118582.

**Ziegler, J. F.; Ziegler, M. D.; Biersack, J. P.** (**2010**): SRIM – The stopping and range of ions in matter (2010). In: *Nuclear Instruments and Methods in Physics Research Section B: Beam Interactions with Materials and Atoms* 268, 11-12, S. 1818–1823. DOI: 10.1016/j.nimb.2010.02.091.